

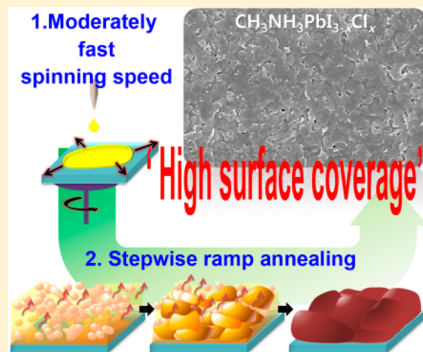
Optimized Organometal Halide Perovskite Planar Hybrid Solar Cells via Control of Solvent Evaporation Rate

Rira Kang, Jeung-Eun Kim, Jun-Seok Yeo, Sehyun Lee, Ye-Jin Jeon, and Dong-Yu Kim*

Heeger Center for Advanced Materials (HCAM), School of Materials Science and Engineering, Gwangju Institute of Science and Technology, Gwangju 500-712, Republic of Korea

Supporting Information

ABSTRACT: Organometallic halide perovskite-based solar cells have exhibited rapidly increasing efficiencies through the use of mesoporous composites. The addition of materials used in organic solar cells to perovskite-based solar cells (PSCs) enables the fabrication of low-cost, flexible, low-temperature, solution-processed PSCs. However, obtaining sufficient coverage of the organic layer, usually poly(3,4-ethylenedioxythiophene)-poly(styrenesulfonate) (PEDOT:PSS), with $\text{CH}_3\text{NH}_3\text{PbI}_{3-x}\text{Cl}_x$ films remains difficult in spite of the advances. In this study, we investigated the influence of controlling the solvent evaporation rate on the degree of PEDOT:PSS surface coverage by $\text{CH}_3\text{NH}_3\text{PbI}_{3-x}\text{Cl}_x$. We determined that an adequately fast spinning speed, drying at room temperature, and stepwise ramp annealing are critical for obtaining optimized planar hybrid perovskite solar cells with an ITO/PEDOT:PSS/ $\text{CH}_3\text{NH}_3\text{PbI}_{3-x}\text{Cl}_x$ /PCBM/Al structure and efficiencies of up to 11.8%.



INTRODUCTION

Methylammonium lead halide ($\text{CH}_3\text{NH}_3\text{PbX}_3$, X = Cl, Br, I) and its mixed-halide perovskites ($\text{CH}_3\text{NH}_3\text{PbI}_{3-x}\text{Cl}_x$, $\text{CH}_3\text{NH}_3\text{PbI}_{3-x}\text{Br}_x$) have attracted much attention for photovoltaic devices owing to their light absorption properties, long-term charge life, low cost, and facile fabrication with a solution-processing technique.^{1–9} From a pillar-structured device with mesoporous TiO_2 (mp- TiO_2),^{3–8} structural changes to perovskite-based solar cells (PSCs) have progressed through meso-superstructured devices with an insulating Al_2O_3 scaffold^{10,11} and planar-structured devices with compact TiO_2 (c- TiO_2).^{12–14} Among the methylammonium lead-based perovskites, $\text{CH}_3\text{NH}_3\text{PbI}_3$ exhibits the best results when used in a mp- TiO_2 structured device owing to the fact that the diffusion length of electrons is relatively shorter than that of holes, and the current is irregularly produced throughout the grains.¹⁵ $\text{CH}_3\text{NH}_3\text{PbI}_{3-x}\text{Cl}_x$ is considered a desirable perovskite material for planar-structured device owing to its ability to generate a uniform current throughout the grains¹⁵ and its comparable effective diffusion length for both electrons and holes.^{15–17} Vapor-deposited $\text{CH}_3\text{NH}_3\text{PbI}_{3-x}\text{Cl}_x$ in a planar-structured device with compact TiO_2 exhibited a PCE of 15.4%.¹²

It was recently found that adopting the concept of organic photovoltaics (OPVs)^{18–21} in PSCs facilitates the flexible fabrication of low-temperature solution-processed PSCs.^{20,22} Yang et al. showed that PSCs with poly(3,4-ethylenedioxythiophene)-poly(styrenesulfonate) (PEDOT:PSS) as a hole transporting layer and phenyl-C₆₁-butyric acid methyl ester (PCBM) as an electron transporting layer when using spin-coated $\text{CH}_3\text{NH}_3\text{PbI}_{3-x}\text{Cl}_x$ as a light absorber exhibited PCE values of more than 11%.²² These planar hybrid-structured

PSCs (ph-PSCs) can overcome the limitations of previous PSC structures such as their low perovskite pore-filling fraction⁸ and the need for high-temperature processing sintering TiO_2 ,⁵ and expensive vacuum techniques.¹² Even though the morphology of perovskite films has been studied as a function of parameters such as initial precursor concentration, the kinds of solvents used,¹⁸ and the time and temperature of annealing,²³ wide morphological variation has resulted in significant differences in the photovoltaic performance of PSCs, regardless of differences in device structures and fabrication techniques.¹⁴ For sufficient coverage of the surface, it is essential to evaporate the solvent the instant the film is spin coated because the perovskite film is extremely sensitive to ambient conditions until it is completely crystallized.

In this work, we controlled spinning speeds (1500 and 3000 rpm) and carried out different annealing conditions (room temperature drying, stepwise ramp, and rapid annealing type) to gain insight into the influence of the solvent evaporation rate on the surface coverage of PEDOT:PSS by $\text{CH}_3\text{NH}_3\text{PbI}_{3-x}\text{Cl}_x$ for the optimization of photovoltaic performance in ph-PSCs. $\text{CH}_3\text{NH}_3\text{PbI}_{3-x}\text{Cl}_x$ films spin coated at 1500 rpm were strongly dependent on different annealing type, whereas we found that $\text{CH}_3\text{NH}_3\text{PbI}_{3-x}\text{Cl}_x$ films spin coated at 3000 rpm were less affected by different annealing type. We suggested that solvent evaporation rate can contribute to the crystallization process of $\text{CH}_3\text{NH}_3\text{PbI}_{3-x}\text{Cl}_x$ films. The high surface coverage was obtained by spin coating at

Received: August 7, 2014

Revised: October 16, 2014

Published: October 23, 2014



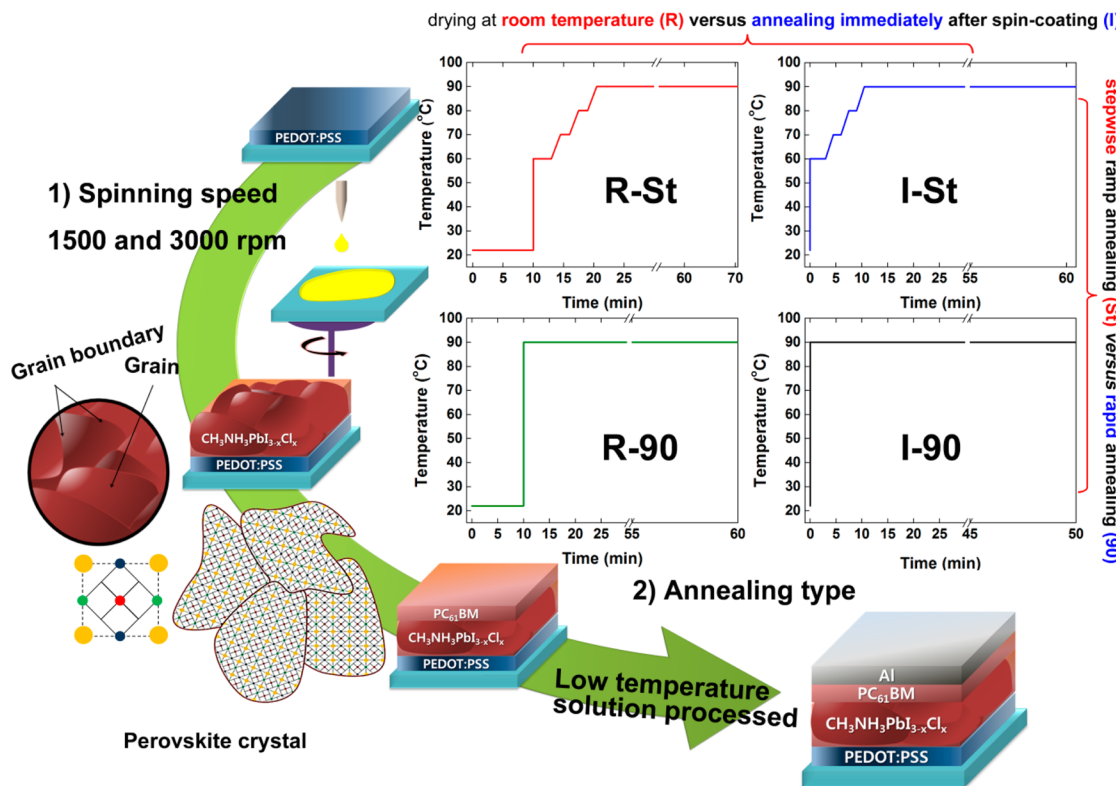


Figure 1. Process steps for the fabrication of planar hybrid solar cells via the control of (1) spin-coating spinning speed and (2) four annealing types.

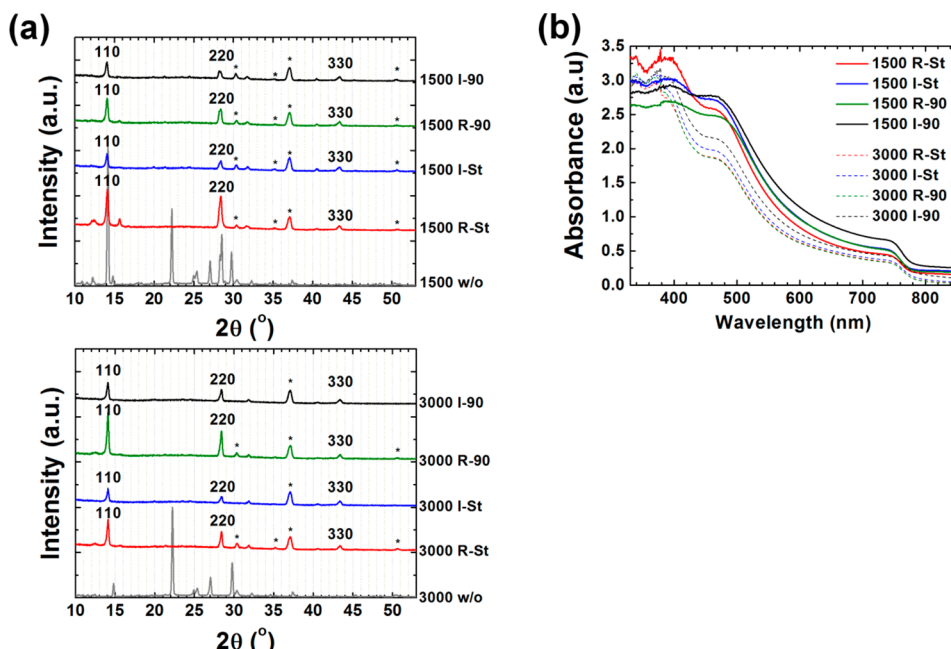


Figure 2. (a) XRD patterns and (b) UV-vis spectra of $\text{CH}_3\text{NH}_3\text{PbI}_{3-x}\text{Cl}_x$ films spin coated on PEDOT:PSS at 1500 and 3000 rpm, followed by four different annealing processes. The asterisks (*) indicate the ITO substrate and the gray lines represent unannealed films.

moderately fast spin coating, drying at room temperature, and annealing with stepwise ramp type.

EXPERIMENTAL SECTION

Device Fabrication. Figure 1 shows the process steps of our device fabrication. To fabricate the device, indium–tin oxide (ITO)-coated glass substrates (Samsung Corning Co.,

Ltd.) were cleaned with acetone, distilled water, and isopropyl alcohol in an ultrasonic bath. The precleaned ITO substrates were UV-ozone treated for 20 min, and then poly(3,4-ethylenedioxythiophene)–poly(styrenesulfonate) (PEDOT:PSS, Clevios AI 4083) with a thickness of ~60 nm was spin coated onto the ITO substrates at 5000 rpm for 40 s, followed by annealing at 100 °C for 20 min in air. As the light-harvesting

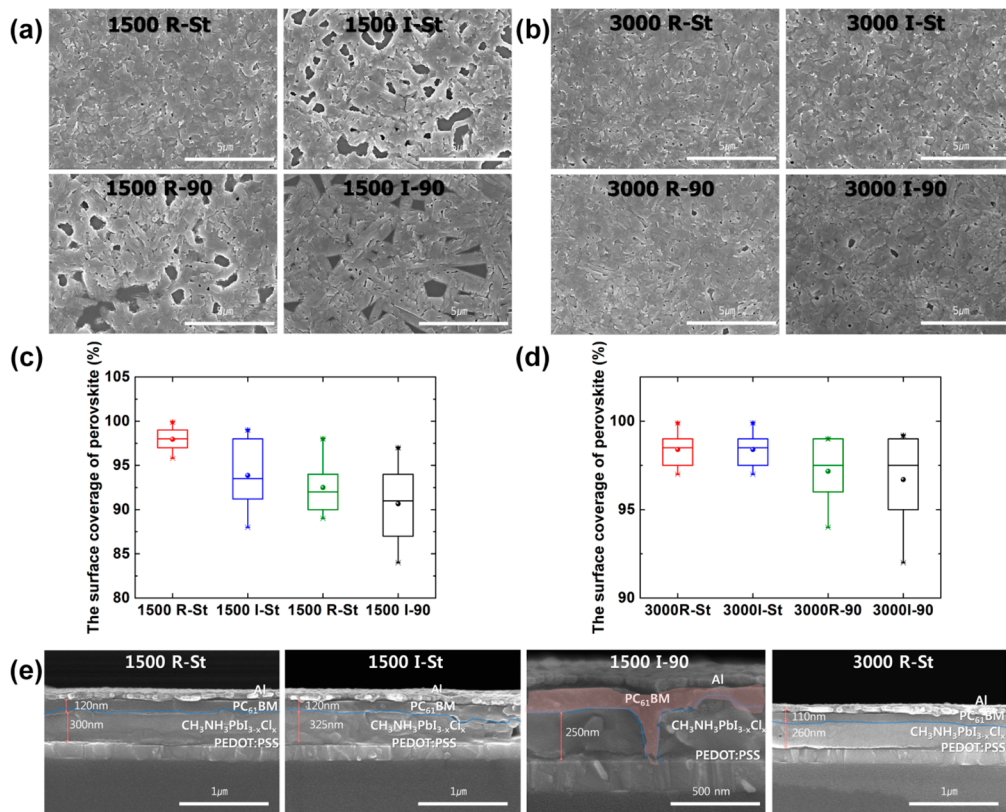


Figure 3. SEM images and the surface coverage of 35 wt % $\text{CH}_3\text{NH}_3\text{PbI}_{3-x}\text{Cl}_x$ films spin coated on PEDOT:PSS at (a, c) 1500 and (b, d) 3000 rpm for the four annealing types. (e) Cross-sectional SEM images of devices with $\text{CH}_3\text{NH}_3\text{PbI}_{3-x}\text{Cl}_x$ films.

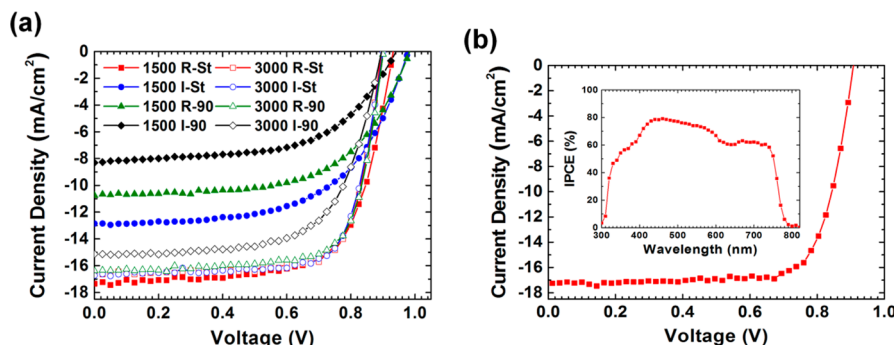


Figure 4. J – V characteristics of solar cell devices with $\text{CH}_3\text{NH}_3\text{PbI}_{3-x}\text{Cl}_x$ films spin coated at (a) 1500 and 3000 rpm, followed by four different annealing processes in a single batch. (b) The sample showing the best performance (inset: external quantum efficiency of the device with PCE = 11.8%; the integrated short-circuit current is 17.16 mA/cm²).

layer, 35 wt % $\text{CH}_3\text{NH}_3\text{PbI}_{3-x}\text{Cl}_x$ was spin coated from a dimethylformamide (DMF) solution with $\text{CH}_3\text{NH}_3\text{I}$ (synthesized in a previous study) and PbCl_2 (Aldrich) in a 3:1 molar ratio, followed by four different annealing processes in a N_2 -filled glovebox. After the annealing process, $\text{CH}_3\text{NH}_3\text{PbI}_{3-x}\text{Cl}_x$ films were rapidly cooled to room temperature. Twenty milligrams of phenyl-C61-butrylic acid methyl ester (PCBM, Nano-C) in 1 mL of chloroform:chlorobenzene (1:1) with a thickness of \sim 110 nm was spin coated onto the perovskite layer in a N_2 -filled glovebox. Aluminum (80 nm thick) was thermally deposited onto the PCBM layer under vacuum at 10^{-6} Torr. The area of the device was 4.64 mm^2 . The J – V characteristics of the devices were measured with a Keithley 4200 instrument under 100 mA cm^{-2} illumination from a 1 kW Oriel solar simulator with an AM 1.5 G filter in air. A calibrated

silicon reference solar cell with a KG5 filter certified by the National Renewable Energy Laboratory (NREL) was used to confirm the measurement conditions. The devices were scanned from 1.2 to -1 V at a scan rate of 0.275 V/s. To measure the hysteresis, the devices were scanned from 1.2 to -1 V (forward) or from -1 to 1.2 V (reverse) at the same scan rate.

Material Characterization. The surface coverage of the perovskite from SEM images was calculated by using the threshold function in the ImageJ program. The X-ray diffraction patterns were detected with Bruker advance 8 k. The UV-visible absorption spectra of the perovskite films were recorded with a PerkinElmer Lambda 12 UV/Visible Spectrophotometer (HP 8453). The SEM images were obtained with a Hitachi S-4700 microscope.

RESULTS AND DISCUSSION

In Figure 1, we show the fabrication process of ph-PSCs, which consisted of PEDOT:PSS transporting holes to the indium tin oxide (ITO) and PCBM transporting electrons to the aluminum electrode. We also show four graphs of the different annealing types. A 35 wt % precursor solution ($\text{CH}_3\text{NH}_3\text{I}:\text{PbCl}_2 = 3:1$ molar ratio) in dimethylformamide (DMF) was spin coated onto a PEDOT:PSS layer in a N_2 -filled glovebox to investigate the influence of the solvent evaporation rate on the morphology of the $\text{CH}_3\text{NH}_3\text{PbI}_{3-x}\text{Cl}_x$ film. The suitable precursor concentrations were 35 wt % for an optimized device. The influence of precursor solution concentration and spinning speeds on the coverage of the surface, the layer thickness, and the photovoltaic performance are shown in the Supporting Information (2.1. Concentration and the spinning speeds section).

For the control of solvent evaporation, the $\text{CH}_3\text{NH}_3\text{PbI}_{3-x}\text{Cl}_x$ films spin coated on PEDOT:PSS at 1500 and 3000 rpm were annealed in a N_2 -filled glovebox with use of four

different methods: two stepwise ramp types, denoted as R-St and I-St, and two rapid types, denoted as R-90 and I-90, shown in Figure 1. The final annealing temperature was fixed at 90 °C for 50 min. To confirm the phase transformation of $\text{CH}_3\text{NH}_3\text{I}$ and PbCl_2 into $\text{CH}_3\text{NH}_3\text{PbI}_{3-x}\text{Cl}_x$ in the treated films, X-ray diffraction (XRD) patterns are shown in Figure 2a. The peaks at 14.06°, 28.40°, and 43.30° are respectively assigned to the (110), (220), and (330) planes, and there are no peaks for PbCl_2 or the additional formation of PbI_2 for all the $\text{CH}_3\text{NH}_3\text{PbI}_{3-x}\text{Cl}_x$ films, indicating good conversion from the precursors to perovskite.²³

Scanning electron microscopy (SEM) images and the surface coverage of $\text{CH}_3\text{NH}_3\text{PbI}_{3-x}\text{Cl}_x$ spin coated on PEDOT:PSS as a function of the two spin-coating rotation speeds and four annealing types are shown in Figure 3. Our treatments, which are related to the control of solvent evaporation, seemed to have an effect not on crystal domain sizes but on the surface coverage. Particularly, the coverage of the $\text{CH}_3\text{NH}_3\text{PbI}_{3-x}\text{Cl}_x$ films spin coated at 1500 rpm was significantly dependent on the different annealing types (R-St, I-St, R-90, and I-90); 1500 R-St exhibited relatively higher surface coverage, whereas 1500 I-St, R-90, and I-90 exhibited uncovered PEDOT:PSS areas, and the average surface coverage decreased from 1500 R-St to I-90; for 1500 I-90, needle-like crystallites were dominant. The cross-sectional SEM images (Figure 3e) are similar to the surface images; 1500 R-St is relatively homogeneous (refer to Table S4, Supporting Information), whereas 1500 I-St exhibits gaps between both the bottom and top perovskite layers and some pinholes (1500 R-90 is similar to 1500 I-St, data not shown). The many pinholes in 1500 I-90 show that PCBM was in contact with PEDOT:PSS through the uncovered PEDOT:PSS surface. This suggests that (1) natural drying at

Table 1. Photovoltaic Parameters of Planar Hybrid Perovskite Solar Cells in a Single Batch

		V_{oc} (V)	J_{sc} (mA/cm ²)	FF (%)	PCE (%)
1500	R-St	0.93	17.26	68	10.93
	I-St	0.98	12.87	58	7.37
	R-90	0.98	10.71	60	6.34
	I-90	0.94	8.28	57	4.46
3000	R-St	0.89	16.60	74	11.01
	I-St	0.90	16.66	74	11.06
	R-90	0.90	16.38	73	10.80
	I-90	0.89	15.22	65	8.83

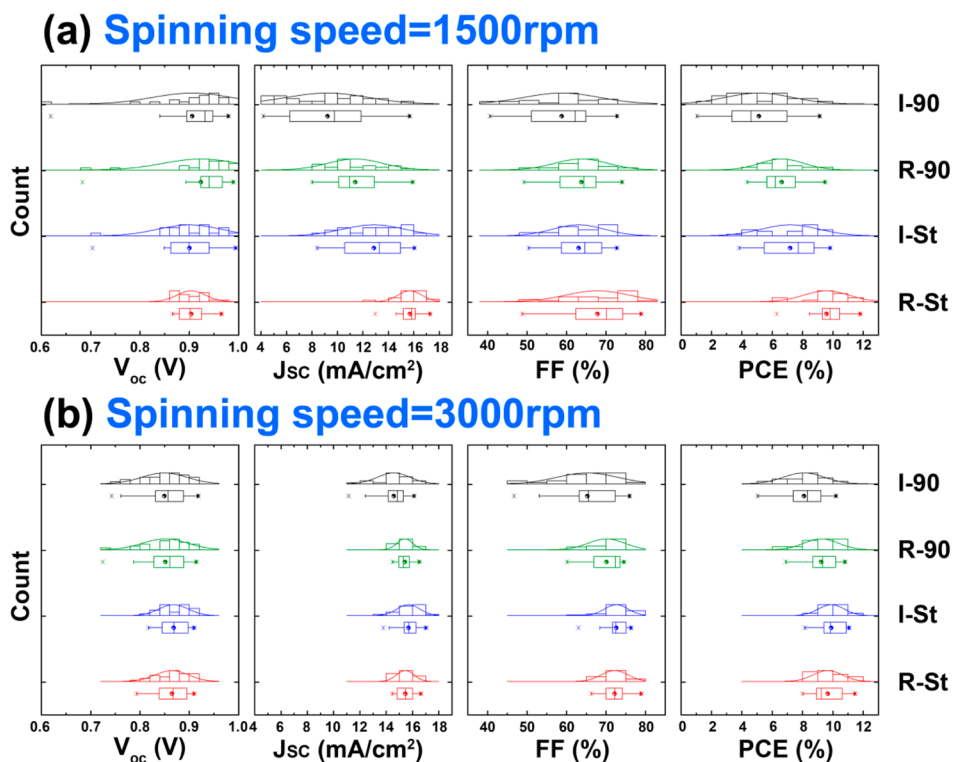


Figure 5. Histograms and skeletal box-and-whisker plots (the elements of skeletal box-and-whisker plots are illustrated in the Supporting Information) of photovoltaic parameters in ph-PSCs with $\text{CH}_3\text{NH}_3\text{PbI}_{3-x}\text{Cl}_x$ films spin coated at (a) 1500 and (b) 3000 rpm, followed by four different annealing processes.

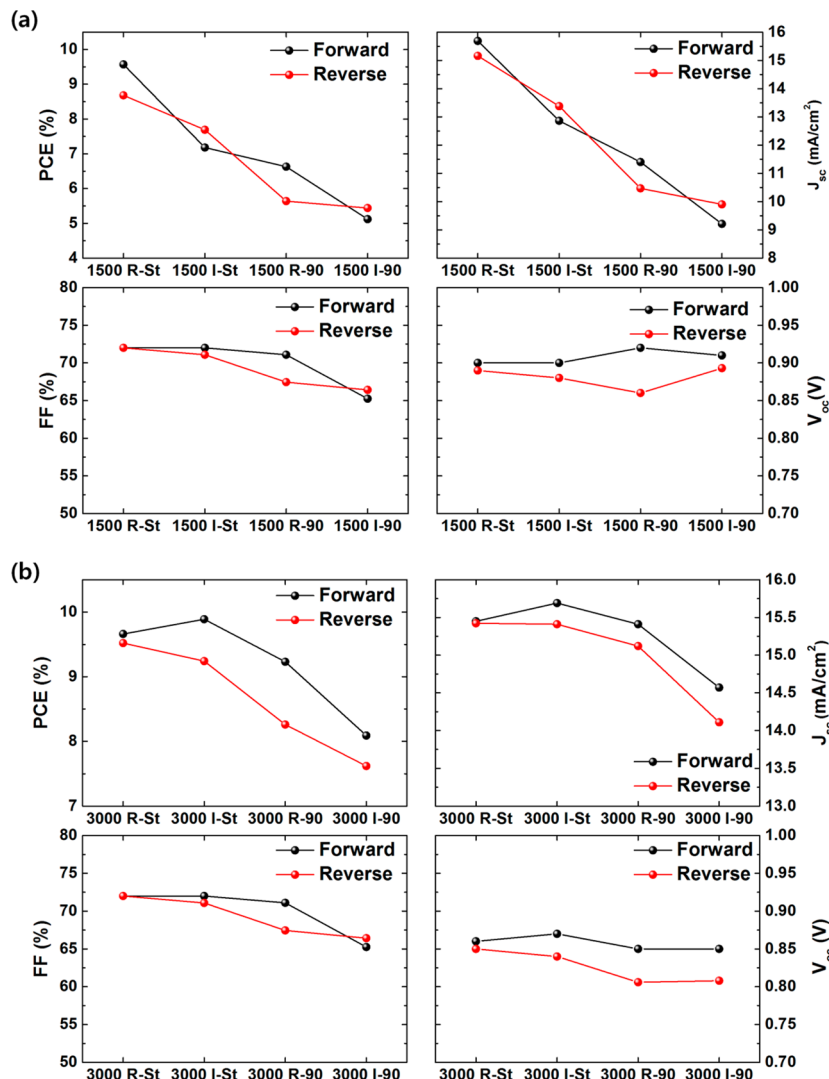


Figure 6. Average photovoltaic parameters of planar hybrid perovskite solar cells with $\text{CH}_3\text{NH}_3\text{PbI}_{3-x}\text{Cl}_x$ films spin coated on PEDOT:PSS at (a) 1500 and (b) 3000 rpm as a function of scanning direction.

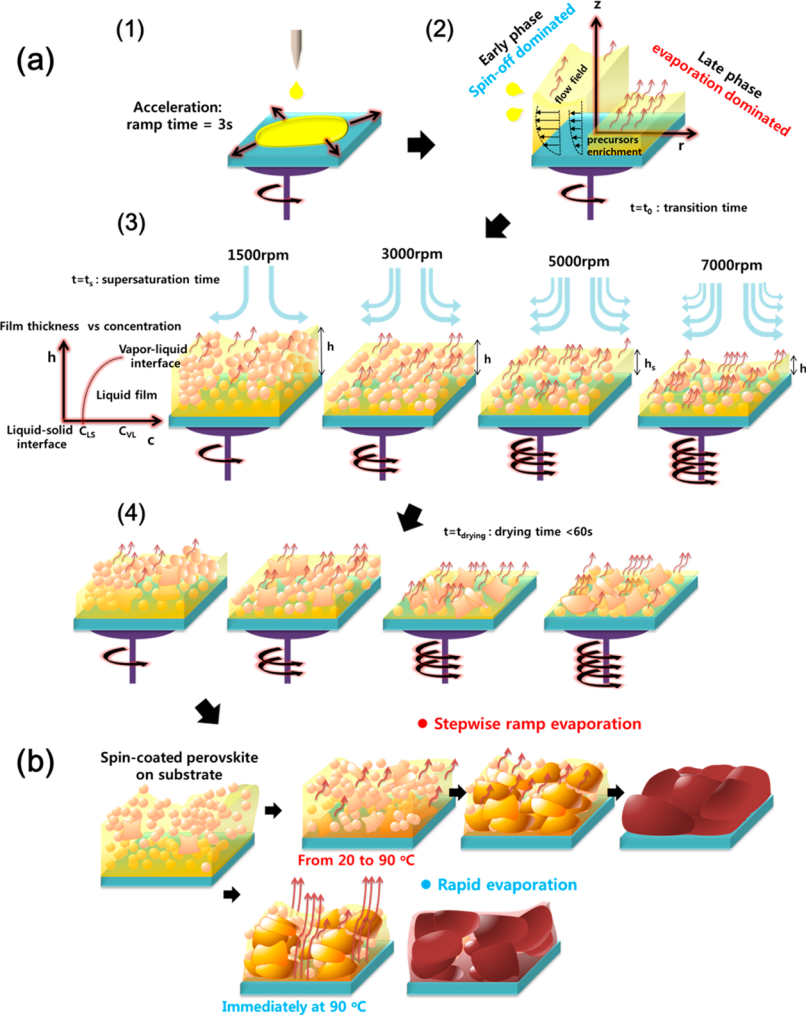
room temperature (example: 1500 R-St versus I-St) and (2) stepwise ramp annealing (1500 R-St versus R-90) promote high surface coverage as opposed to immediately annealing the films at 90 °C after spin coating.

The morphology in the case of $\text{CH}_3\text{NH}_3\text{PbI}_{3-x}\text{Cl}_x$ films spin coated at 3000 rpm was less vulnerable to different annealing types, even though the average of surface coverage decreased slightly from 3000 R-St to 3000 I-90. These results indicate that appropriately fast spin coating is primarily responsible for sufficient surface coverage. Moreover, 3000 R-St is quite uniform in the cross-sectional SEM image. The results for 3000 I-St, R-90, and I-90 are similar to those for 3000 R-St (data not shown).

The $J-V$ curves and photovoltaic performance parameters for a single batch of devices are shown in Figure 4a and Table 1, respectively. Histograms and the skeletal box-and-whisker plots of photovoltaic performance parameters for 50 devices per each condition are also shown in Figure 5. For films spin coated at 1500 rpm, PCE decreased from 10.93% to 4.46% as a function of the different annealing types. The faster a solvent is evaporated during thermal annealing, the more J_{sc} decreases, in this case from 17.26 to 8.28 mA/cm². This tendency of J_{sc} clearly corresponds to the surface coverage shown in Figure 3c and the

UV-vis spectra shown in Figure 2b. The results indicate that the incident light not absorbed by perovskite may pass directly through uncovered regions. Despite the decrease of J_{sc} , only V_{oc} for 1500 I-St, R-90, and I-90 with pinholes increased. The increases of V_{oc} can be explained by the fact that the contact between PEDOT:PSS and PCBM through pinholes can lead to the creation of a Schottky junction, as mentioned in a recent report,²⁴ even though it is generally known that insufficient surface coverage leads to shunt paths in PSCs with TiO₂ and Spiro-OMeTAD.¹² All the performance parameters of films spin coated at 1500 rpm are widespread, as shown in Figure 5a, owing to a relatively rough surface (from 300 to 385 nm, shown in Table S4, Supporting Information) and low surface coverage; however, the device prepared by 1500 R-St showed the best performance (Figure 4b), with $V_{oc} = 0.91$ V, $J_{sc} = 17.27$ mA/cm², fill factor (FF) = 75%, and PCE = 11.80%. Although all the photovoltaic parameters of the devices were influenced by scanning direction, which is well-known in perovskite photovoltaic devices,²⁵ there was no trend of the average photovoltaic parameters influenced by scanning direction probably due to the rough surface of the films spin coated at 1500 rpm (Figure 6).

For films spin coated at 3000 rpm, the photovoltaic performance of 3000 R-St was the same as that of 3000 I-St

Scheme 1. Film Formation (a) during Spin Coating at Different Spinning Speeds^a and (b) after Spin Coating^b

^aStages: (1) the precursor solution is placed onto the substrate; (2) spin-coating showing the dominate processes in the early and late stages, followed by reaching a transition thickness; (3) the solution becomes supersaturated with a thickness of h_s ; (4) nucleation and growth occur during the drying time. ^bThe samples are subjected to stepwise ramp and rapid thermal annealing.

(PCE = ~11%), and the PCEs of **3000 R-90** and **I-90** were respectively 10.80% and 8.83%, as shown in Figure 4a. For the stepwise ramp annealed perovskite films (**3000 R-St** and **I-St**), the photovoltaic performance was almost the same, whereas the rapidly annealed perovskite films (**3000 R-90** and **I-90**) exhibited slightly decreased performance, as shown in Figure 5. These results are also consistent with the SEM images, the surface coverage, and the UV-vis spectra. Even if the J_{sc} and V_{oc} values of films spin coated at 3000 rpm decreased slightly because the film was relatively thinner than that of films spin coated at 1500 rpm, the best performance of films spin coated at 3000 rpm was comparable with that of **1500 R-St**, and the photovoltaic performance of films spin coated at 3000 rpm was significantly less distributed than that of films spin coated at 1500 rpm, resulting from a smooth surface and high surface coverage. The average photovoltaic parameters were significantly influenced by scanning direction, except **3000 R-St** (Figure 6).

We investigated the influence of the spinning speed on the $\text{CH}_3\text{NH}_3\text{PbI}_{3-x}\text{Cl}_x$ film formation in terms of sufficient surface coverage. The crystallization mechanism of solution-deposited perovskite is still unclear. The precursor solution deposited

onto PEDOT:PSS was accelerated to each final spin speed for 3 s (Scheme 1a-1). The $\text{CH}_3\text{NH}_3\text{PbI}_{3-x}\text{Cl}_x$ film formation as a function of the ramping time is described in the Supporting Information (2.2. Ramping time section). The thickness of the resulting films decreased because of the centrifugal forces in the early stage and the evaporation of the solvent in the later stage (Scheme 1a-2). The evaporative thinning is dependent on the low vapor pressure of DMF.²⁶ After a transition point, in which hydrodynamic thinning gives way to evaporative thinning, the concentration of the precursors near the liquid–vapor (L–V) interface is higher owing to the predominant evaporative thinning; the solution finally becomes supersaturated (Scheme 1a-3). After supersaturation, the precursors begin to aggregate (nucleation and growth) during the later stage of spinning (Scheme 1a-4).²⁷

After spin coating, the $\text{CH}_3\text{NH}_3\text{PbI}_{3-x}\text{Cl}_x$ films fully cover the surface of the PEDOT:PSS layer, regardless of the spinning speed (Figure S3, Supporting Information). The spinning speed ($\omega^{-2/3}$) also has a relatively weaker effect on the surface coverage than the concentration (C_0), based on eq 1 in the Supporting Information. These results indicate that drying or thermal annealing after spin coating mainly influence the surface coverage.

Films spin coated at 5000 and 7000 rpm, which were almost independent of the annealing type (data not shown), exhibited complete coverage of the PEDOT:PSS surface and incomplete coverage of the outer surface before and after the annealing of R-St (Figures S1b and S3, Supporting Information). The incomplete coverage of the outer surface can be explained by considering the relation between N and $\omega^{-2/3}$ in eq 1 (refer to the Supporting Information). It is suggested that with the rapid spinning speed, stable nuclei form quickly and the rate of growth is faster than that with a spinning time of 60 s. The results for films spin coated at 3000 rpm can be explained by the fact that the spinning speed provides sufficient precursors to completely cover both the PEDOT:PSS surface and the outer surface. Films spin coated at 3000 rpm are slightly dependent on annealing types because DMF is suitably evaporated and stable nuclei can form in 60 s. On the other hand, the surface coverage of films spin coated at 1500 rpm is considerably dependent on the different annealing types (Figure 3b). The results imply that with a slow spinning speed, the solution can become supersaturated near the liquid–vapor interface, whereas elsewhere in the solution the degree of supersaturation is insufficient to overcome the energy barrier for nucleation during a spinning time of 60 s mainly because of the thickness of the film. Therefore, drying at room temperature and stepwise ramp annealing at low temperatures (<90 °C) after spin coating is particularly important for nucleation and growth in order to avoid pinholes, especially for the thicker films. It is unclear whether nucleation starts at the L–V interface or the liquid–solid (L–S) interface because nucleation is determined by the concentration gradient, which can be changed by the evaporation rate, the diffusion coefficient of the precursors in the liquid film, and the precursor–PEDOT:PSS interactions. Thus, the kinetics of nucleation and growth play a crucial role in the final morphology.

In particular, the drying at room temperature and the thermal annealing type both contribute to the nucleation and growth processes for thicker films, as mentioned above. High surface coverage is attainable by both drying at room temperature and stepwise ramp annealing (Figure 3). Although the distinction between drying at room temperature and stepwise ramp annealing from 60 to 90 °C is uncertain in terms of nucleation and growth processes, the influence of the four annealing types on $\text{CH}_3\text{NH}_3\text{PbI}_{3-x}\text{Cl}_x$ films is illustrated in Scheme 1b by dividing them into stepwise ramp and rapid annealing. We suggest that nucleation and growth start at low temperatures during drying at room temperature and continue during stepwise ramp annealing (the thermal energy at each temperature defines nucleation, directly determining the final film) and that this treatment provides sufficient time for densification to avoid pinholes.²⁸ However, in rapid annealing there is rapid grain growth and evaporation of excess precursors without sufficient time for densification, which may result in both pinholes and intraholes through the films.²⁸ Complete crystallization is thermodynamically achieved only during annealing at the higher thermal temperatures (>90 °C) following processing at low temperature (<90 °C). Hence, control of the solvent evaporation rate is considered a key parameter for fabricating films with high surface coverage.

CONCLUSION

In conclusion, we investigated the influence of the solvent evaporation rate as a function of different spin-coating speeds and annealing types on $\text{CH}_3\text{NH}_3\text{PbI}_{3-x}\text{Cl}_x$ films with high

surface coverage in planar hybrid perovskite solar cells based on ITO/PEDOT:PSS/ $\text{CH}_3\text{NH}_3\text{PbI}_{3-x}\text{Cl}_x$ /PCBM/Al. A $\text{CH}_3\text{NH}_3\text{PbI}_{3-x}\text{Cl}_x$ film with high surface coverage is achievable with moderately fast spin coating, drying at room temperature, and stepwise ramp annealing. High reproducibility in the performance parameters and a PCE of up to 11.80% could be accomplished by using the optimized $\text{CH}_3\text{NH}_3\text{PbI}_{3-x}\text{Cl}_x$ film. Further investigation would be necessary in order to understand the effect of the substrate type on surface coverage and the precise crystallization mechanism.

ASSOCIATED CONTENT

Supporting Information

The elements of skeletal box-and-whisker plots, SEM images, *J*–*V* characterization, thickness and performance parameters of devices with spin-coated $\text{CH}_3\text{NH}_3\text{PbI}_{3-x}\text{Cl}_x$ films as a function of different concentrations of the precursor solution, the spinning speeds, and the ramping times. This material is available free of charge via the Internet at <http://pubs.acs.org>.

AUTHOR INFORMATION

Corresponding Author

*E-mail: kimdy@gist.ac.kr.

Notes

The authors declare no competing financial interests.

ACKNOWLEDGMENTS

This work was supported by National Research Foundation of Korea (NRF) grants funded by the Ministry of Science, ICT & Future Planning (MISP, No. 2013-059210).

REFERENCES

- (1) Kojima, A.; Teshima, K.; Shirai, Y.; Miyasaka, T. Organometal Halide Perovskites as Visible-Light Sensitizers for Photovoltaic Cells. *J. Am. Chem. Soc.* **2009**, *131*, 6050–6051.
- (2) Cheng, Z.; Lin, J. Layered Organic–Inorganic Hybrid Perovskites: Structure, Optical Properties, Film Preparation, Patterning and Templating Engineering. *CrystEngComm* **2010**, *12*, 2646–2662.
- (3) Snaith, H. J. Perovskites: The Emergence of a New Era for Low-Cost, High-Efficiency Solar Cells. *J. Phys. Chem. Lett.* **2013**, *4*, 3623–3630.
- (4) Kim, H. S.; Im, S. H.; Park, N.-G. Organolead Halide Perovskite: New Horizons in Solar Cell Research. *J. Phys. Chem. C* **2014**, *118*, 5615–5625.
- (5) Etgar, L.; Gao, P.; Xue, Z.; Peng, Q.; Chandiran, A. K.; Liu, B.; Nazeeruddin, M. K.; Grätzel, M. Mesoscopic $\text{CH}_3\text{NH}_3\text{PbI}_3/\text{TiO}_2$ Heterojunction Solar Cells. *J. Am. Chem. Soc.* **2012**, *134*, 17396–17399.
- (6) Kim, H.-S.; Lee, C.-R.; Im, J.-H.; Lee, K.-B.; Moehl, T.; Marchioro, A.; Moon, S.-J.; Humphry-Baker, R.; Yum, J.-H.; Moser, J. E. Lead Iodide Perovskite Sensitized All-Solid-State Submicron Thin Film Mesoscopic Solar Cell with Efficiency Exceeding 9%. *Sci. Rep.* **2012**, *2*, 591.
- (7) Burschka, J.; Pellet, N.; Moon, S.-J.; Humphry-Baker, R.; Gao, P.; Nazeeruddin, M. K.; Grätzel, M. Sequential Deposition as a Route to High-Performance Perovskite-Sensitized Solar Cells. *Nature* **2013**, *499*, 316–319.
- (8) Leijtens, T.; Lauber, B.; Eperon, G. E.; Stranks, S. D.; Snaith, H. J. The Importance of Perovskite Pore Filling in Organometal Mixed Halide Sensitized TiO_2 -based Solar Cells. *J. Phys. Chem. Lett.* **2014**, *5*, 1096–1102.
- (9) Lee, M. M.; Teuscher, J.; Miyasaka, T.; Murakami, T. N.; Snaith, H. J. Efficient Hybrid Solar Cells Based on Meso-Superstructured Organometal Halide Perovskites. *Science* **2012**, *338*, 643–647.

- (10) Ball, J. M.; Lee, M. M.; Hey, A.; Snaith, H. J. Low-Temperature Processed Meso-Superstructured to Thin-Film Perovskite Solar Cells. *Energy Environ. Sci.* **2013**, *6*, 1739–1743.
- (11) Carnie, M. J.; Charbonneau, C.; Davies, M. L.; Troughton, J.; Watson, T. M.; Wojciechowski, K.; Snaith, H.; Worsley, D. A. A One-Step Low Temperature Processing Route for Organolead Halide Perovskite Solar Cells. *Chem. Commun.* **2013**, *49*, 7893–7895.
- (12) Liu, M.; Johnston, M. B.; Snaith, H. J. Efficient Planar Heterojunction Perovskite Solar Cells by Vapour Deposition. *Nature* **2013**, *501*, 395–398.
- (13) Chen, Q.; Zhou, H.; Hong, Z.; Luo, S.; Duan, H.-S.; Wang, H.-H.; Liu, Y.; Li, G.; Yang, Y. Planar Heterojunction Perovskite Solar Cells via Vapor Assisted Solution Process. *J. Am. Chem. Soc.* **2013**, *136*, 622–625.
- (14) Eperon, G. E.; Burlakov, V. M.; Docampo, P.; Goriely, A.; Snaith, H. J. Morphological Control for High Performance, Solution-Processed Planar Heterojunction Perovskite Solar Cells. *Adv. Funct. Mater.* **2014**, *24*, 151–157.
- (15) Edri, E.; Kirmayer, S.; Henning, A.; Mukhopadhyay, S.; Gartsman, K.; Rosenwaks, Y.; Hodes, G.; Cahen, D. Why Lead Methylammonium Tri-Iodide Perovskite-Based Solar Cells Require a Mesoporous Electron Transporting Scaffold (but Not Necessarily a Hole Conductor). *Nano Lett.* **2014**, *14*, 1000–1004.
- (16) Xing, G.; Mathews, N.; Sun, S.; Lim, S. S.; Lam, Y. M.; Grätzel, M.; Mhaisalkar, S.; Sum, T. C. Long-Range Balanced Electron-and Hole-Transport Lengths in Organic-Inorganic $\text{CH}_3\text{NH}_3\text{PbI}_3$. *Science* **2013**, *342*, 344–347.
- (17) Stranks, S. D.; Eperon, G. E.; Grancini, G.; Menelaou, C.; Alcocer, M. J.; Leijtens, T.; Herz, L. M.; Petrozza, A.; Snaith, H. J. Electron-Hole Diffusion Lengths Exceeding 1 Micrometer in an Organometal Trihalide Perovskite Absorber. *Science* **2013**, *342*, 341–344.
- (18) Jeng, J. Y.; Chiang, Y. F.; Lee, M. H.; Peng, S. R.; Guo, T. F.; Chen, P.; Wen, T. C. $\text{CH}_3\text{NH}_3\text{PbI}_3$ Perovskite/Fullerene Planar-Heterojunction Hybrid Solar Cells. *Adv. Mater.* **2013**, *25*, 3727–3732.
- (19) Sun, S.; Salim, T.; Mathews, N.; Duchamp, M.; Boothroyd, C.; Xing, G.; Sum, T. C.; Lam, Y. M. The Origin of High Efficiency in Low-Temperature Solution-Processable Bilayer Organometal Halide Hybrid Solar Cells. *Energy Environ. Sci.* **2014**, *7*, 399–407.
- (20) Malinkiewicz, O.; Yella, A.; Lee, Y. H.; Espallargas, G. M.; Graetzel, M.; Nazeeruddin, M. K.; Bolink, H. J. Perovskite Solar Cells Employing Organic Charge-Transport Layers. *Nat. Photonics* **2014**, *8*, 128–132.
- (21) Docampo, P.; Ball, J. M.; Darwich, M.; Eperon, G. E.; Snaith, H. J. Efficient Organometal Trihalide Perovskite Planar-Heterojunction Solar Cells on Flexible Polymer Substrates. *Nat. Commun.* **2013**, *4*, 2761.
- (22) You, J.; Hong, Z.; Yang, Y.; Chen, Q.; Cai, M.; Song, T.-B.; Chen, C.-C.; Lu, S.; Liu, Y.; Zhou, H. Low-Temperature Solution-Processed Perovskite Solar Cells with High Efficiency and Flexibility. *ACS Nano* **2014**, *8*, 1674–1680.
- (23) Dualeh, A.; Tétreault, N.; Moehl, T.; Gao, P.; Nazeeruddin, M. K.; Grätzel, M. Effect of Annealing Temperature on Film Morphology of Organic–Inorganic Hybrid Pervoskite Solid-State Solar Cells. *Adv. Funct. Mater.* **2014**, *24*, 3250–3258.
- (24) Wang, Q.; Dong, Q.; Xiao, Z.; Yuan, Y.; Huang, J. Large Fill-Factor Bilayer Iodine Perovskite Solar Cells Fabricated by Low-Temperature Solution-Process. *Energy Environ. Sci.* **2014**, *7*, 2359–2365.
- (25) Snaith, H. J.; Abate, A.; Ball, J. M.; Eperon, G. E.; Leijtens, T.; Noel, N. K.; Stranks, S. D.; Wang, J. T.-W.; Wojciechowski, K.; Zhang, W. Anomalous Hysteresis in Perovskite Solar Cells. *J. Phys. Chem. Lett.* **2014**, *5*, 1511–1515.
- (26) Toolan, D. T.; Pullan, N.; Harvey, M. J.; Topham, P. D.; Howse, J. R. In Situ Studies of Phase Separation and Crystallization Directed by Marangoni Instabilities During Spin-Coating. *Adv. Mater.* **2013**, *25*, 7033–7037.
- (27) Ghani, F. *Nucleation and Growth of Unsubstituted Metal Phthalocyanine Films from Solution on Planar Substrates*. Ph.D. Dissertation, Universitätsbibliothek Potsdam, Germany, 2013.
- (28) Bassiri-Gharb, N.; Bastani, Y.; Bernal, A. Chemical Solution Growth of Ferroelectric Oxide Thin Films and Nanostructures. *Chem. Soc. Rev.* **2014**, *43*, 2125–2140.